UDK 004.942: 669.058.67 ISSN 1580-2949
Original scientific article/Izvirni znanstveni članek Mater. Tehnol.

NUMERICAL SIMULATION OF WC-Co PARTICLE DEPOSITION BY HVOF SPRAYING

NUMERIČNA SIMULACIJA NANAŠANJA WC-Co DELCEV S POSTOPKOM NAPRŠEVANJA HVOF

Xianghui Qi, Nianchu Wu*
School of Mechanical Engineering, Liaoning Petrochemical University, Fushun 113001, P.R. China

Prejem rokopisa – received: 2024-09-30; sprejem za objavo – accepted for publication: 2025-02-24

doi:10.17222/mit.2024.1323

WC-Co coatings exhibit the unsurpassed wear resistance needed to maximize the wear resistance of various technological components, thus expanding their service lives and prolonging product lifespans. HVOF thermal spraying is an established coating process that offers advantages such as low porosity, low oxide content and strong adhesion in the final products. Finite element modeling was utilized to study both the deformation behavior of particles and the bonding mechanisms following impacts of WC-Co particles in various states with the substrate during HVOF spraying. Numerical results demonstrate that velocity has a more significant effect on impact deformation than temperature. Furthermore, particles at high temperatures and velocities exhibit higher degrees of deformation and higher bonding rates after impact. Additionally, as particle diameter increases, both the compression and flattening rates decrease, and the time required to bond with the substrate increases.

Keywords: WC-Co coating, HVOF, bonding mechanism, numerical simulation classification

WC-Co prevleke so glede odpornosti proti obrabi neprekosljive. Njihova odlična odpornost proti obrabi je potrebna za izdelavo različnih zahtevnih tehnoloških komponent pri katerih si želimo čim daljšo dobo trajanja in čim manj popravil. Termični postopek naprševanja HVOF (angl.: High Velocity Oxygen Fuel) je uveljavljen postopek izdelave prevlek, ki omogoča izdelavo gostih prevlek z majhno poroznostjo, majhno vsebnostjo kisika in močno adhezijo s podlago končnega izdelka. Avtorji v tem članku opisujejo uporabo metode končnih elementov (MKE) za študij deformacije WC-Co delcev in njihove vezave med udarjanjem na podlago pri različnih procesnih parametrih HVOF. Rezultati numeričnih analiz so pokazali, da hitrost udarjanja delcev kovine bolj vpliva na njihovo deformacijo kot njihova temperatura. Nadalje, pri visokih temperaturah in hitrostih imajo delci višjo stopnjo deformacije in višjo hitrost vezave na podlago. Dodatno, z naraščanjem premera delcev se zmanjšujeta tako njihov tlak, kot tudi stopnja sploščitve in posledično čas potreben za kohezijo delcev s podlago narašča.

Ključne besede: WC-Co prevleke, HVOF, mehanizem vezave, numerična simulacija, klasifikacija

1 INTRODUCTION

Cemented carbide (WC-Co) displays impressive wear resistance due to its exceptional hardness and fracture toughness.[1–3] At present, WC-Co metal surface coatings are being employed to increase the wear resistance of various engineering components, including those utilized for machining operations and fluid control valve internals, oil and gas drilling, and mining.[4,5] There are numerous techniques for depositing WC-Co surface coatings. The WC-Co coatings produced with the cold spraying methods of Andrew Siao Ming Ang[6] and Giovanni Bolelli[7,8] exhibit high porosity, which consequently diminishes their mechanical and corrosion resistance properties. The use of the air plasma spraying method, as employed by F. Ghadami[9,10] in the preparation of WC-Co coatings, resulted in particle oxidation due to their exposure to high temperatures during flight. As a result, the oxide content of coatings increased and corrosion resistance decreased, affecting their use in environments with high corrosion risks.

Direct energy deposition coatings deposited using Erica Liverani's method[11,12] consistently exhibit pores and cracks along the length of their thickness. High velocity oxygen fueling (HVOF) has proven itself useful across numerous industries due to its broad scope of applications, high efficiency, superior quality coating production and cost effectiveness.[13–16] HVOF powder spraying represents the pinnacle of thermal spraying metal coatings. In contrast to the speeds of approximately 100 m/s (flame spraying) to 1000 m/s (plasma spraying), this process employs a combination of fuels, including paraffin. Burning them with sufficient oxygen generates a flame with an approximate melting temperature of 3000 °C and velocity of up to 2000 m/s. Under the conditions of high velocity and low temperature, the resulting coating is characterized by a high degree of density and adhesion, with minimal oxidation of the particles. Residue particles within the coating show little sign of oxidization. The HVOF technology can be applied to various powder forms; however, its primary focus lies in hard, wear-resistant coatings, where adhesion is key. The HVOF method produces thicker coatings with lower po-

---

*Corresponding author's e-mail:
wunianchu@163.com (Nianchu Wu)

© 2025 The Author(s). Except when otherwise noted, articles in this journal are published under the terms and conditions of the Creative Commons Attribution 4.0 International License (CC BY 4.0).

rosity, lower oxide content, and higher adhesion, as it creates coatings with fewer residual stresses than plasma spraying.[17–19]

Powder particles' characteristics and spraying process parameters greatly affect the coating performance. Although experimental methods can yield highly reliable results, the process of observation is challenging when attempting to investigate their relationship. As the reaction process is short and requires rapid measurement techniques, some parameters, such as the particle temperature prior to the substrate contacting the particles, can be hard to assess accurately. Additionally, the applicability of the results is limited to a particular spraying system. Some important spraying process parameters, such as the nozzle size and powder type, can be altered, and then the results obtained with the original experiment have no reference value if a different spraying system is used. Furthermore, the analytical skills required to interpret the results are inadequate. The deformation of particles and the substrate during coating formation due to impacts are difficult or impossible to monitor and study in detail. Furthermore, the experimental cost is considerable. It can thus be concluded that the experimental method has numerous shortcomings in the study of the high-velocity oxygen fuel (HVOF) process. Numerical simulation and modelling are key to cutting costs while simultaneously improving real-time monitoring of reaction processes. The use of numerical simulation software enables an examination of the powder particle behavior during collisional bonding to the substrate surface, as well as the observation of the stresses and strains that occur during coating deposition.[20–22]

To provide a reference basis for the actual spraying process, this study employs numerical simulation to examine the effects of different WC-Co particle speeds, temperatures, and diameters of particles, assess how they affect deformation and how well particles combine with the substrate as the quality of this combination is also affected by the above factors.

Table 1: WC-Co particles and 304 substrate[26]

Material parameters	WC-Co	304 stainless steel
Density (kg·m^{-3})	14000	7896
Melting point (K)	1580	1696
Thermal conductivity (W·m^{-1}·K^{-1})	36	16
Specific heat (J·kg^{-1}·K^{-1})	295	446
Young's modulus (GPa)	500	217.5
Poisson's ratio	0.27	0.33
Shear modulus (GPa)	197	81.8
Static shear strength A (MPa)	1550	793
Strain-hardening modulus B (MPa)	2200	510
Strain rate sensitive coefficient C	0.0312	0.014
Strain-hardening exponent n	0.45	0.26
Thermal softening exponent m	1.34	1.03
Reference temperature (K)	298	298
Reference equivalent plastic strain rate (s^{-1})	1	1
Inelastic heat share	0.9	0.9

2 MODEL DEVELOPMENT

This research investigates solid impact dynamics by employing the commercial finite element solver ABAQUS/Explicit. The model incorporates strain hardening, thermal softening, friction heating from frictional contact between two materials, plastic dissipation, and plastic deformation as key variables in impact dynamics simulations. Given the minute size and brief reaction times involved in HVOF processes (on the micrometer scale and nanosecond timescale, respectively), the heat transfer from particles to the substrate can generally be overlooked, suggesting that an adiabatic heating process occurs instead. **Table 1** provides details regarding the material properties available within these models as well as material properties of each material type.

The linear elastic model provides an effective means of exploring various impact scenarios using elastic response properties of the material. Equation 1 shows how it correlates with the Johnson-Cook plasticity model:[23–25]

$$\sigma = (\varepsilon_{\mathrm{p}}, \dot{\varepsilon}, T) = \left[A + B(\varepsilon_{\mathrm{p}})^{n}\right](1 + C \ln \dot{\varepsilon}^{*})\left[1 - (T^{*})^{m}\right] \quad (1)$$

where A is the static shear strength, B is the strain-hardening modulus, C is the strain-rate sensitive coefficient, n is the strain-hardening exponent, m is the thermal softening exponent, ε_{P} is the average plastic shear strain, while $\dot{\varepsilon}^{*}$ and T^{*} are dimensionless variables,[11] specifically defined as shown in Equations (2), (3):

$$\dot{\varepsilon}^{*} = \frac{\dot{\varepsilon}}{\dot{\varepsilon}_{0}} \quad (2)$$

$$T^{*} = \frac{T - T_{\mathrm{r}}}{T_{\mathrm{m}} - T_{\mathrm{r}}} \quad (3)$$

Here, $\dot{\varepsilon}$ is the equivalent plastic strain rate, $\dot{\varepsilon}_{0}$ is the reference equivalent plastic strain rate, T is the material temperature, T_{r} is the material reference temperature, and T_{m} is the material melting temperature, also known as the liquid phase line.[25]

Figure 1 shows that an impact process can be represented as a three-dimensional (3D) domain for computational efficiency and cost considerations. Given that the collision between particles and the matrix occurs axisymmetrically, it is possible to utilize one quarter of the 3D model for the numerical simulation. The larger model allows for more detailed observation of the collision results. In our finite element model, the substrate's diameter and height are approximately 10and 7 times those of the particles, while the grid size for both the particles and the matrix is one-thirtieth of the particle size, providing computational efficiency at low costs. The face-to-face contact algorithm is used for the outer surface of the particle and the upper surface of the substrate; symmetric constraints are used for the side of the particle

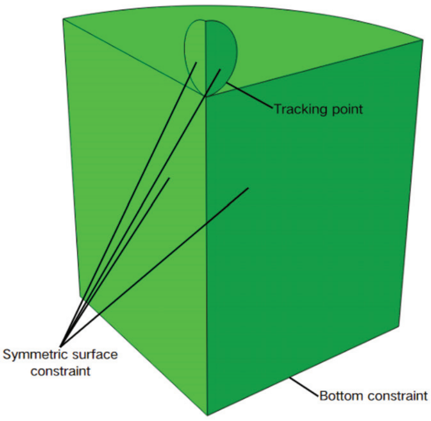

Figure 1: Three-dimensional domain in impact process

and the substrate; complete constraints are used for the lower surface of the substrate. As evidenced by the mesh sensitivity analysis, shear flow localization and material heating are predominantly influenced by the mesh size.[27] The selection of tracking nodes involves the identification of locations where strong plastic deformation could take place on impacting particles' surfaces, as shown in **Figure 1**. In general, tracking nodes provide the maximum values of the plastic strain, flow stress and temperature change over time.

3 RESULTS AND DISCUSSION

A simulation was conducted to model the impact of WC-Co particles on a substrate made of 304 stainless steel at 298 K. The results revealed the influence of three factors – temperature, particle shape and velocity, and particle diameter. Particles with a 30 μm diameter served as reference particles to assess the effects of temperature and impact velocity on particle deformation. An optimal set of parameters was selected to investigate their influence on the particle size deformation.

3.1 Dynamic deformation behavior upon particle-substrate impacts

This study investigates the dynamic deformation behavior of 30-μm-diameter WC-Co particles upon impact with the 304 stainless steel substrate. Based on the research by S. Gu et al.,[26] the initial velocity and temperature were set to 500 m/s and 800 K while the substrate temperature was 298 K (room temperature). **Figure 2** depicts the cloud diagram of the maximum plastic strain at different stages throughout the dynamic deformation of 30-μm-diameter WC-Co particles impacting with the 304 stainless steel substrate. As seen in **Figure 2**, the maximum plastic strain increases rapidly during the initial 20 nanoseconds (ns) of the impact process, leading to deformed particles. After 40 ns, however, the increase slows down, and the deformation begins to stabilize as the impact-induced deformation reaches a steady state. At 80 ns, the WC-Co particles exhibit a flattened morphology, with a concave downward curvature in the central region and material sputtering outward and upward at the edges. They are embedded within the 304 stainless steel substrate, forming pits and establishing bonding. The edges of these pits display a slight upward curvature.

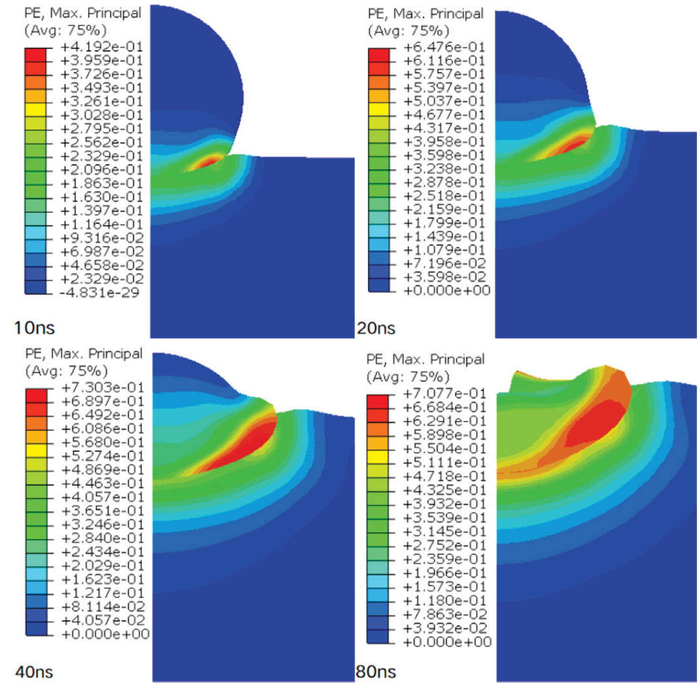

Figure 2: Dynamic deformation upon particle impact

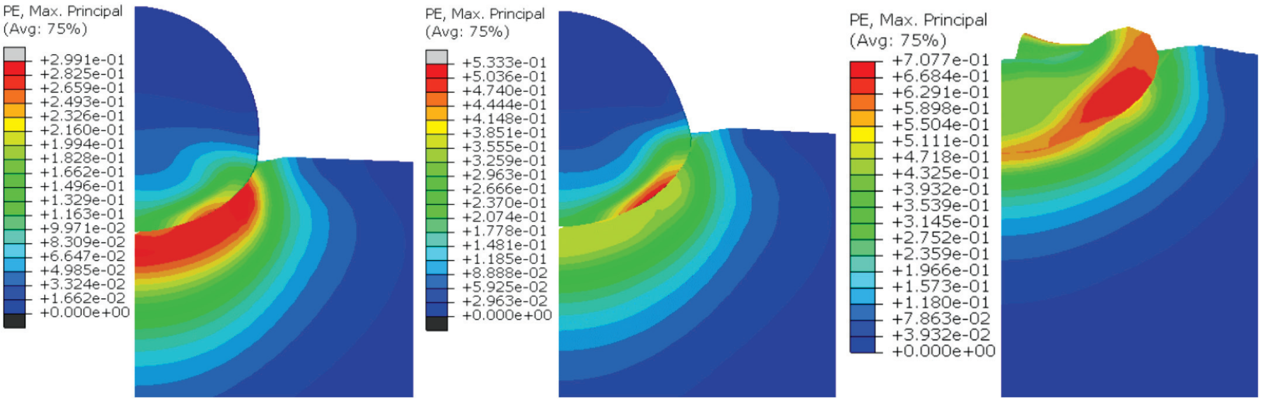

Figure 3: Maximum plastic strain of particles traveling at different velocities (300 m/s, 400 m/s, 500 m/s from left to right)

3.2 Effect of particle velocity on particle deposition behavior

This section explores the effect of particle velocity on particle deposition behavior by setting the temperature to 800 K, using velocities of 300–500 m/s for three separate batches, and fixing the diameter of all particles at 30 μm. **Figure 3** depicts this distortion; as shown here, the initial velocity has an enormously significant influence on the deformation of both the particles and the substrate. The maximum plastic strain and degree of particle deformation show significant variations with the increased velocity when analyzed for deformation at 300 m/s and 400 m/s. Further investigation revealed that the maximum plastic strain did not occur at the point of impact between the particles and substrate, but rather within the inner parts of the substrate's crater edge and the lower edge of the particle. However, despite the high plastic strain, no bonding with the substrate occurred, and a rebound phenomenon was observed. Upon reaching a velocity of 500 m/s, the maximum plastic strain increased; there was no rebound, the particles underwent significant deformation, and they were integrated into the matrix.

Figures 4 and **5** illustrate the temperature and flow stress readings obtained at the tracking point during the most intense reaction. As the particle velocity increases to 300 m/s and 400 m/s, the temperature increases as well, together with the corresponding increase in the flow stress. This reaches its maximum within 20 ns, being below the melting point of WC-CO. Consequently, there is no adiabatic shear instability, and the particles cannot bond with the substrate. At 500 m/s the temperature rises sharply until reaching its WC-Co melting point within 20 ns. This is followed by the melting of the inner edge of the particles. As the flow stress approaches zero and shear instability occurs, the deformation mechanism changes from plastic to viscous deformation. At this stage, the particles begin to adhere to their matrix and bond with it.

3.3 Effect of particle temperature on particle deposition behavior

In contrast to cold spraying, HVOF employs combustion of gas as the energy source for particle movement. As they reach and impact their target substrate, the colli-

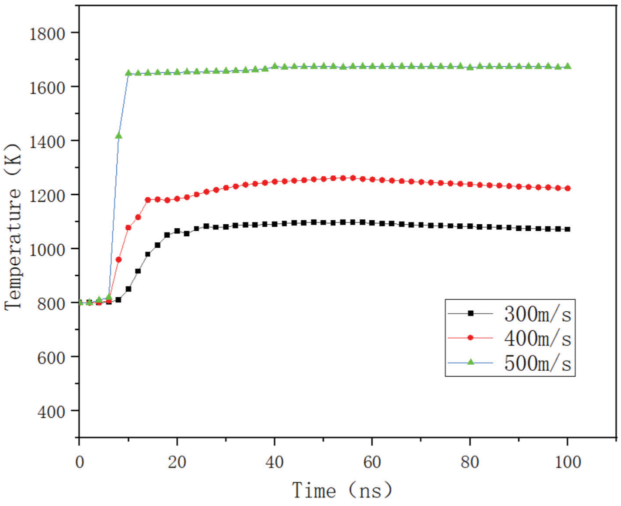

Figure 4: Temperature variations for particles traveling at different velocities

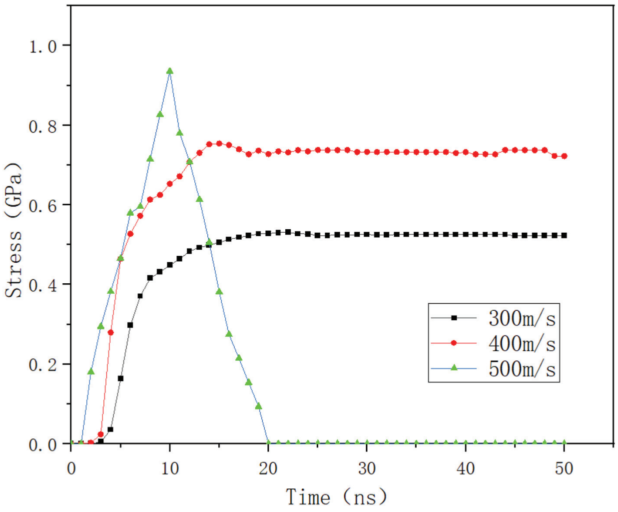

Figure 5: Changes in flow stress of particles at different velocities

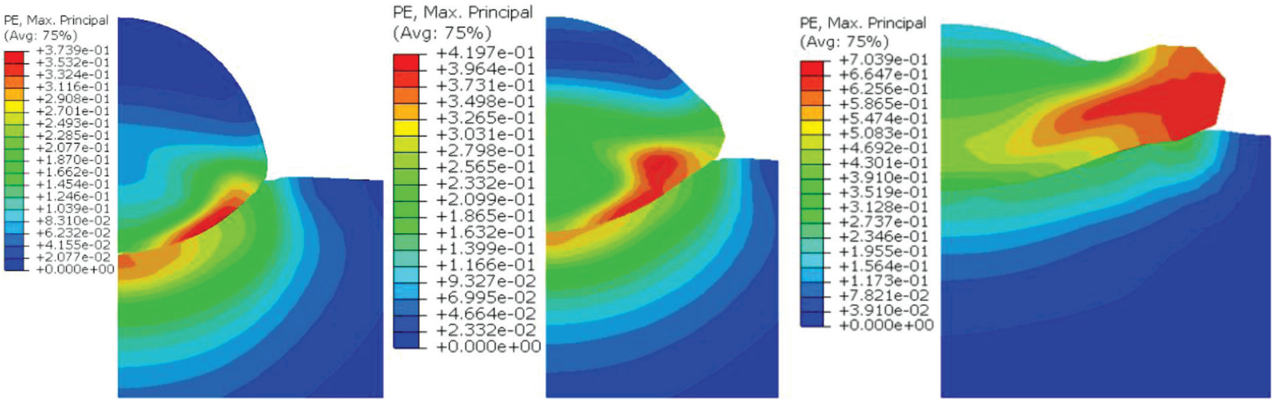

Figure 6: Maximum plastic strain of particles at different temperatures (1000 K, 1200 K, 1300 K from left to right)

sion results show correlations between the particle temperature/velocity, and successful bonding processes. For the purpose of this study, the diameter, velocity and temperature are assumed to be 30 µm, 300 m/s, and (1000, 1200 and 1300) K, respectively. These values are used to establish which factor exerts more influence. The resulting particle deformation is illustrated in **Figure 6**, which shows that the maximum plastic strain increases with temperature, leading to enhanced deformation. A comparison of particle deformation at different temperatures illustrates this effect. However, particle deformation due to velocity variations was much greater.

The temperature data at the point of the highest reaction intensity were collected and subsequently examined in accordance with the methodology illustrated in **Figure 7**. Upon reaching 1000 K during this reaction, the temperature shows an increase by 300 K. Similarly, at temperatures of 1200 K and 1300 K, an increase of 300 K is observed. Under constant velocity, the temperature rise is also constant from the beginning to the end of the reaction. By comparison, a change in the velocity (from 300 m/s to 500 m/s) causes larger temperature fluctuations, with a temperature increase of 600 K. **Figure 8** shows the flow stress at the tracking point, reaching its maximum value within 20 ns at 1000 K and 1200 K. The change in the flow stress is more pronounced at 1300 K, reaching its maximum value within 10 ns as the particles begin to melt. In 20 ns, the flow stress gradually decreases to 0. A comparison with the conditions including 500 m/s and 800 K from **Figure 4** reveals a reduction in both the magnitude of the change and the peak value.

In conclusion, the amount of thermal energy generated across a broad range of particle impact temperatures is nearly identical. The temperature increase remains consistent as the impact thermal energy is generated by the particles with the same diameter and velocity, indicating that the kinetic energy plays a crucial role in shaping the particle behavior before the impact. To further enhance HVOF coating quality, it would be advantageous to prioritize velocity over temperature.

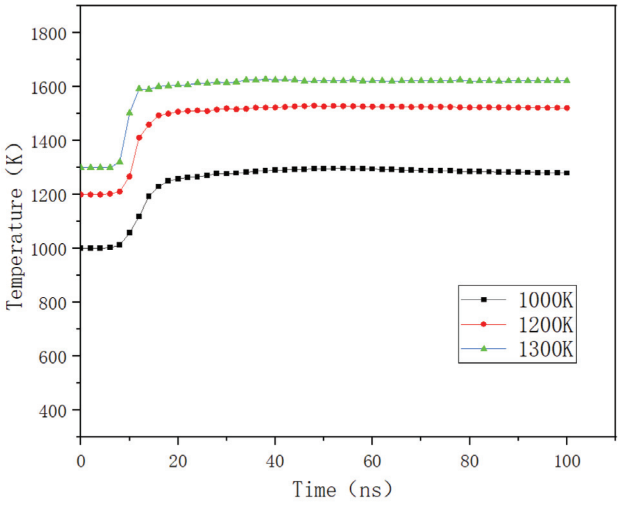

Figure 7: Particle temperature change over time at different temperatures

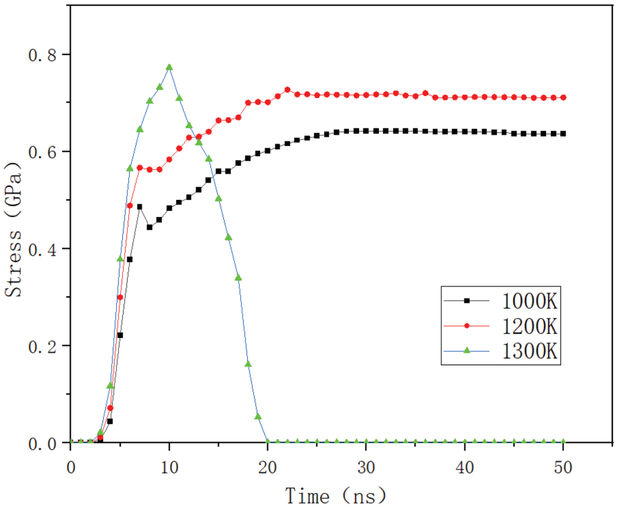

Figure 8: Flow stress changes in particles at different temperatures

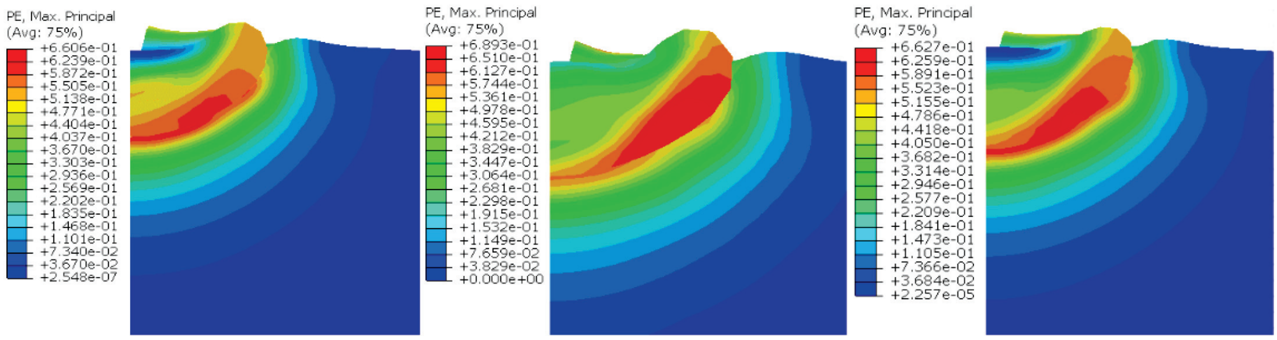

Figure 9: Maximum plastic strain at different particle diameters (20 µm, 30 µm, 40 µm from left to right)

3.4 Effect of particle size on particle deposition behavior

In the preceding two sections, the particle velocity of 500 m/s, temperature of 800 K, and particle diameters of (20, 30, and 40) µm were selected for the investigation of how the particle size affects impact deformation. **Figure 9** displays the maximum plastic strain over multiple particle diameters, demonstrating that the maximum plastic strain exhibits minimal variation with the changes in particle diameter.

The areas inside the matrix pit were observed to determine edge effects. The particles' lower edge, which contained all the maximum values, exhibited the strongest impact deformation, as illustrated in **Figure 10**. The reaction times were observed and analyzed. **Figure 10** illustrates that particles with a diameter of 20 µm reach the maximum plastic strain in 30 ns, while particles with a diameter of 30 µm reach the maximum plastic strain in 50 ns, and particles with a diameter of 40 µm reach the maximum plastic strain in 70 ns. This suggests that larger particle sizes increase the time required for bonding.

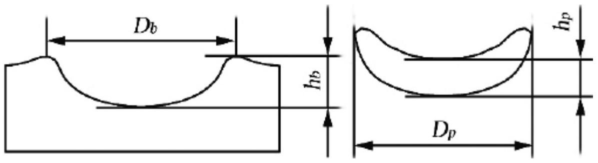

Figure 11: Diagram on the left shows 304 stainless steel matrix while diagram on the right shows WC-Co particles

Figure 11 identifies and defines relevant geometric dimensions of the matrix pit and deformed particles from **Figure 9**. The particles have an initial diameter *D*. The deformation of the matrix pit is normalized by the particle diameter to D_b and h_b, or D_b/D and H_b/D. Here, D_b is the diameter of the matrix pit, h_b is its depth, D_p is the particles' diameter after impact deformation, and H_b is the particles' central thickness after impact deformation. The flat rate R_f and the compression rate R_c represent the deformation of the particles. The following formulas can be used to determine both the flat rate and the compression rate.

$$R_f = \frac{D_p}{D} \tag{4}$$

$$R_c = 1 - \frac{h_p}{D} \tag{5}$$

Table 2 provides accurate values of normalization parameters so that we can analyze the substrate crater deformation induced by the impacts of various-sized WC-Co particles with the 304 stainless steel substrate.

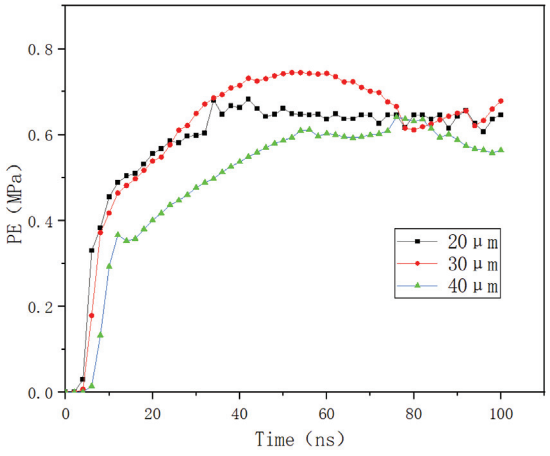

Figure 10: Plastic strain variations over time with different particle diameters

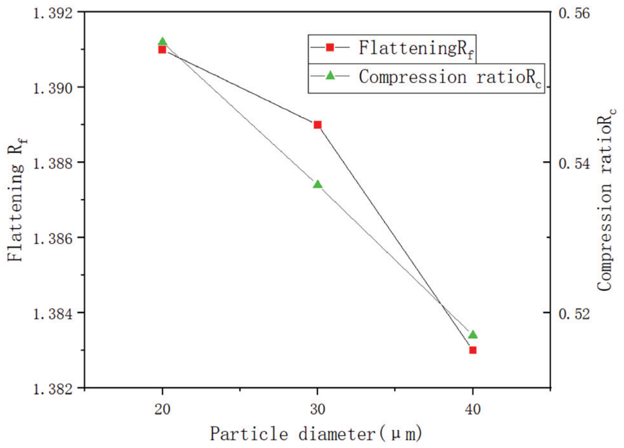

Figure 12: Flatness and compression for different particle diameters

Figure 12 depicts flattening and compression rates for deformed particles.

Table 2: Normalized parameters of pit deformation, including deformed-particle flattening and compression rates

D (µm)	Stainless steel matrix
20	1.667 0.519
30	1.685 0.519
40	1.667 0.519

A study of **Figure 10** and **Table 2** suggests that an increase in the particle size results in longer bonding times. This indicates that large-size particles are not conducive to their bonding with the matrix. **Table 2** shows that the normalized parameters for the base pit, exhibiting the deformation due to the particles being in contact with the substrate, are nearly the same for a variety of particle sizes. Furthermore, the degree of deformation of the base pit has no impact on the particle size.

4 CONCLUSIONS

This study utilizes numerical simulation to investigate the impact process and deposition behavior of WC-Co particles produced through HVOF using substrate materials. The effects of varying particle diameter, temperature, and velocity were investigated to provide a theoretical basis for optimizing spraying parameters and improving coating quality. The following conclusions are drawn from this research:

(1) When particles do not reach the melting point during impact, they fail to bond with their matrix, resulting in their rebound into the surrounding space. Particles showing low velocity and temperature do not display evidence of adiabatic shear instability.

(2) It is recommended that particle velocity be given greater consideration than temperature to enhance the quality of HVOF coatings. Studies have indicated that high velocity has a significant effect on the deposition behavior of particles.

(3) An increase in particle diameter not only reduces compression and flattening rates, but also prolongs the time required for deposition. Therefore, large particles are not conducive to bonding with the substrate.

Acknowledegnts

This work was supported by the Educational Commission of Liaoning Province of China under Grant No. LJ212410148054, Natural Science Foundation of Liaoning Province under Grant No. 2022-MS-364, and Fushun Revitalization Talents Program under Grant No. FSYC202107011.

5 REFERENCES

[1] J. F. Wang, M. Zhang, R. S. Dai, L. Shao, Z. B. Tu, D. D. Zhu, Z. Z. Xu, S. Dai, L. Zhu, Wear and electrochemical corrosion behaviors of Cu matrix WC-Co reinforced composite coating prepared by cold spray, Surf. Coat. Technol., 488 (**2024**), 131001, doi:10.1016/j.surfcoat.2024.131001

[2] Z. Russell, M. Gaier, M. J. Froning, K. P. Plucknett, The aqueous corrosion and wear responses of HVOF-deposited TiC-Ni3Al, WC-Co, and WC-CoCr coatings on AISI 4130 steel substrates, Surf. Coat. Technol., 473 (**2023**), 130018, doi:10.1016/j.surfcoat.2023.130018

[3] V. Testa, S. Morelli, G. Bolelli, F. Bosi, P. Puddu, A. Colella, T. Manfredini, L. Lusvarghi, Corrosion and wear performances of alternative TiC-based thermal spray coatings, Surf. Coat. Technol., 438 (**2022**), 128400, doi:10.1016/j.surfcoat.2022.128400

[4] A. Tahir, G. R. Li, M. J. Liu, G. J. Yang, C. X. Li, Y. Y. Wang, C. J. Li, Improving WC-Co coating adhesive strength on rough substrate: Finite element modeling and experiment, J. Mater. Sci. Technol., 37 (**2020**), 1–8, doi:10.1016/j.jmst.2019.07.033

[5] D. A. Stewart, P. H. Shipway, D. G. McCartney, Microstructural evolution in thermally sprayed WC–Co coatings: comparison between nanocomposite and conventional starting powders, Acta Mater., 48 (**2000**), 1593–1604, doi:10.1016/S1359-6454(99)00440-1

[6] A. S. Ming Ang, C. C. Berndt, P. Cheang, Deposition effects of WC particle size on cold sprayed WC–Co coatings, Surf. Coat. Technol., 205 (**2011**), 3260–3267, doi:10.1016/j.surfcoat.2010.11.045

[7] G. Bolelli, S. Dosta, L. Lusvarghi, T. Manfredini, J. M. Guilemany, I. G. Cano, Building up WC-Co coatings by cold spray: A finite element simulation, Surf. Coat. Technol., 374 (**2019**), 674–689, doi:10.1016/j.surfcoat.2019.06.054

[8] S. Dosta, G. Bolelli, A. Candeli, L. Lusvarghi, I. G. Cano, J. M. Guilemany, Plastic deformation phenomena during cold spray impact of WC-Co particles onto metal substrates, Acta Mater., 124 (**2017**), 173–181, doi:10.1016/j.actamat.2016.11.010

[9] F. Ghadami, M. H. Sohi, S. Ghadami, Effect of bond coat and post-heat treatment on the adhesion of air plasma sprayed WC-Co coatings, Surf. Coat. Technol., 261 (**2015**), 289–294, doi:10.1016/j.surfcoat.2014.11.016

[10] F. Ghadami, M. H. Sohi, S. Ghadami, Effect of TIG surface melting on structure and wear properties of air plasma-sprayed WC–Co coatings, Surf. Coat. Technol., 261 (**2015**), 108–113, doi:10.1016/j.surfcoat.2014.11.050

[11] E. Liverani, A. Ascari, A. Fortunato, Multilayered WC–Co coatings by Direct Energy Deposition-based cladding: Effect of laser remelting on interface defects, Surf. Coat. Technol., 464 (**2023**), 129556, doi:10.1016/j.surfcoat.2023.129556

[12] A. Fortunato, G. Valli, E. Liverani, A. Ascari, Additive Manufacturing of WC-Co Cutting Tools for Gear Production, Lasers Manuf. Mater. Process., 6 (**2019**), 247–262, doi:10.1007/s40516-019-00092-0

[13] H. S. Sidhu, B. S. Sidhu, S. Prakash, The role of HVOF coatings in improving hot corrosion resistance of ASTM-SA210 GrA1 steel in the presence of Na2SO4–V2O5 salt deposits, Surf. Coat. Technol., 200 (**2006**), 5386–5394, doi:10.1016/j.surfcoat.2005.07.008

[14] N. Behera, M. Srihari, Y. K. Sharma, M. R. Ramesh, An investigation on tribological performance in HVOF sprayed of Amdry1371 and Amdry 1371/WC-Co coatings on Ti6Al4V, Surf. Coat. Technol., 494 (**2024**), 131334, doi:10.1016/j.surfcoat.2024.131334

[15] J. Li, Q. C. Guo, Q. Y. Tang, G. G. Zhao, H. Y. Li, L. F. Ma, Effect of electron beam remelting on microstructure and wear properties of HVOF Ni/WC coatings, Wear, 558–559 (**2024**), 205560, doi:10.1016/j.wear.2024.205560

[16] Y. Y. Li, W. S. Li, W. Y. Li, W. Q. Chen, H. Hong, T. Zhang, Deposition mechanism and fracture characterization of 434 stainless steel HOVF coating on T6061 aluminum alloy, J. Mater. Res. Technol., 32 (**2024**), 3776–3787, doi:10.1016/j.jmrt.2024.08.163

[17] L. Fedrizzi, S. Rossi, R. Cristel, P. L. Bonora, Corrosion and wear behaviour of HVOF cermet coatings used to replace hard chromium, Electrochim. Acta, 49 (**2004**), 2803–2814, doi:10.1016/j.electacta.2004.01.043

[18] X. Z. Wang, H. H. Yao, L. Yuan, L. J. Chen, F. F. Xu, Z. Tan, D. Y. He, Y. G. Yang, Y. B. Liu, Z. Zhou, Novel candidate of metal-based thermal barrier coatings: High-entropy alloy, Surf. Coat. Technol., 474 (**2023**), 130087, doi:10.1016/j.surfcoat.2023.130087

[19] T. Varis, A. Mäkelä, T. Suhonen, J. Laurila, P. Vuoristo, Integrity of APS, HVOF and HVAF sprayed NiCr and NiCrBSi coatings based on the tensile stress-strain response, Surf. Coat. Technol., 452 (**2023**), 129068, doi:10.1016/j.surfcoat.2022.129068

[20] N. Tamanna, R. Crouch, S. Naher, Progress in numerical simulation of the laser cladding process, Opt. Laser. Eng., 122 (**2019**), 151–163, doi:10.1016/j.optlaseng.2019.05.026

[21] X. W. Yang, T. X. Meng, Y. Su, X. X. Chai, Z. G. Guo, T. J. Ma, S. Yin, W. Y. Li, Particle deformation and coating deposition behavior in cold spray additive manufactured aluminum deposit on copper substrate by simulation and experiment, J. Mater. Res. Technol., 30 (**2024**), 2879–2890, doi:10.1016/j.jmrt.2024.04.057

[22] I. Smurov, M. Doubenskaia, A. Zaitsev, Comprehensive analysis of laser cladding by means of optical diagnostics and numerical simulation, Surf. Coat. Technol., 220 (**2013**), 112–121, doi:10.1016/j.surfcoat.2012.10.053

[23] E. Postek, T. Sadowski, Thermomechanical effects during impact testing of WC/Co composite material, Compos. Struct., 241 (**2020**), 112054, doi:10.1016/j.compstruct.2020.112054

[24] S. Zhang, Z. Wang, H. J. Yang, J. W. Qiao, Z. H. Wang, Y. C. Wu, Ultra-high strain-rate strengthening in ductile refractory high entropy alloys upon dynamic loading, Intermet., 121 (**2020**), 106699, doi:10.1016/j.intermet.2020.106699

[25] A. Iturbe, E. Giraud, E. Hormaetxe, A. Garay, G. Germain, K. Ostolaza, P. J. Arrazola, Mechanical characterization and modelling of Inconel 718 material behavior for machining process assessment, Mater. Sci. Eng. A, 682 (**2017**), 441–453, doi:10.1016/j.msea.2016.11.054

[26] S. Kamnis, S. Gu, T. J. Lu, C. Chen, Numerical modeling the bonding mechanism of HVOF sprayed particles, Comput. Mater. Sci., 46 (**2009**), 1038–1043, doi:10.1016/j.commatsci.2009.05.009

[27] Y. Xiao, K. Liu, Penalty-based surface-to-surface contact algorithm for SPH method, Appl. Math. Modell., 117 (**2023**), 359–377, doi:10.1016/j.apm.2022.12.038